

Foreshock sequences and short-term earthquake predictability on East Pacific Rise transform faults

Jeffrey J. McGuire¹, Margaret S. Boettcher² & Thomas H. Jordan³

¹Department of Geology and Geophysics, Woods Hole Oceanographic Institution, and ²MIT-Woods Hole Oceanographic Institution Joint Program, Woods Hole, Massachusetts 02543-1541, USA

³Department of Earth Sciences, University of Southern California, Los Angeles, California 90089-7042, USA

East Pacific Rise transform faults are characterized by high slip rates (more than ten centimetres a year), predominately aseismic slip and maximum earthquake magnitudes of about 6.5. Using recordings from a hydroacoustic array deployed by the National Oceanic and Atmospheric Administration, we show here that East Pacific Rise transform faults also have a low number of aftershocks and high foreshock rates compared to continental strike-slip faults. The high ratio of foreshocks to aftershocks implies that such transform-fault seismicity cannot be explained by seismic triggering models in which there is no fundamental distinction between foreshocks, mainshocks and aftershocks. The foreshock sequences on East Pacific Rise transform faults can be used to predict (retrospectively) earthquakes of magnitude 5.4 or greater, in narrow spatial and temporal windows and with a high probability gain. The predictability of such transform earthquakes is consistent with a model in which slow slip transients trigger earthquakes, enrich their low-frequency radiation and accommodate much of the aseismic plate motion.

On average, before large earthquakes occur, local seismicity rates show a significant increase¹. In continental regions, where dense regional seismic networks provide the best data, most foreshock studies^{2–4}, though not all⁵, are consistent with the hypotheses that earthquake nucleation is independent of magnitude and that foreshocks result from a general triggering process in which there is no fundamental distinction between foreshocks, mainshocks and aftershocks. The inability to distinguish foreshocks from the statistical fluctuations in the continental background seismicity severely limits their usefulness in predicting large earthquakes⁶.

It is unclear, however, whether these statements apply to other tectonic environments, or how aseismic processes affect earthquake triggering. Aseismic slip transients with timescales of days to months have recently been observed in the subduction zones of Japan^{7–9} and Cascadia¹⁰, using continuously monitored GPS arrays. The possibility that aseismic slip triggers large earthquakes on subduction megathrusts is especially intriguing given the observation¹¹ that a slow slip transient occurred 15 minutes before the great 1960 Chilean megathrust earthquake, which had a moment magnitude (M_w) of 9.5, the largest ever recorded. Notably, subduction zones are observed to have higher foreshock rates than continental regions¹².

Another tectonic environment in which aseismic processes are thought to exert a strong influence on fault behaviour is mid-ocean ridge transform faults (RTFs). Studies over the last several decades^{13–15} have shown that on average most of the slip on RTFs, up to about 85% (ref. 15), is aseismic. Moreover, the seismic component of slip occurs in earthquakes that are relatively small ($M_w \leq 7.2$) given the length of the faults^{14–16}. Many of the larger RTF earthquakes are slow events with anomalous low-frequency radiation^{17,18}. Low-frequency spectral analyses^{19,20} have indicated that slow RTF earthquakes are compound events comprising an ordinary rupture and a slow transient of comparable moment but much longer duration; in some cases, the slow component precedes, and presumably initiates, the main seismic component. Time-domain records of slow precursors to RTF earthquakes^{20,21} and episodes of coupled seismic slip observed on adjacent RTFs^{20,22}

support the inference of slow slip transients, but the subject remains controversial²³.

Hydroacoustic detection of foreshocks

Here we use data from a six-element hydroacoustic array deployed by the National Oceanic and Atmospheric Administration's Pacific Marine Environmental Laboratory (NOAA-PMEL) to examine anomalous foreshock sequences on East Pacific Rise (EPR) transform faults (Fig. 1). The NOAA-PMEL arrays^{24–26} routinely locate EPR earthquakes with acoustic source level (ASL) magnitudes (see Methods) M_{ASL} below 3, reducing the detection threshold by 1.5–2.0 magnitude units below global seismicity catalogues (see Methods). A reconnaissance study indicated that foreshocks in the last hour before large events are significantly more common on EPR transform faults than on strike-slip faults in the North Atlantic, Northeast Pacific or Southern California²⁷.

Figure 2 displays stacks of the seismicity in space-time windows centred on nine mainshocks that occurred on the Discovery and Gofar transform faults between May 1996 and December 2001. This set of mainshocks comprised all $M_w \geq 5.4$ earthquakes on these two faults recorded by the NOAA-PMEL array in the Harvard Centroid Moment Tensor (CMT) catalogue²⁸ that did not follow within 1 week and 100 km of another mainshock. The longer window (Fig. 2a) shows low background seismicity tens of hours before the mainshocks and the subsequent aftershock decay. The shorter window (Fig. 2b) reveals an accelerating rate of seismicity close to the mainshock epicentres during the hour immediately preceding the mainshock origin times.

Earthquake triggering model

The anomalous nature of the RTF foreshock activity can be quantified in terms of the Epidemic Type Aftershock Sequence (ETAS) model of triggered seismicity^{4,29,30}. ETAS is a marked point process model³¹ in which all earthquake magnitudes above a lower cutoff m_0 are independent samples of the Gutenberg–Richter (GR) probability distribution, $P(m) = 10^{-b(m-m_0)}$, where b is the slope of the distribution, and all earthquakes give birth to daughter events at

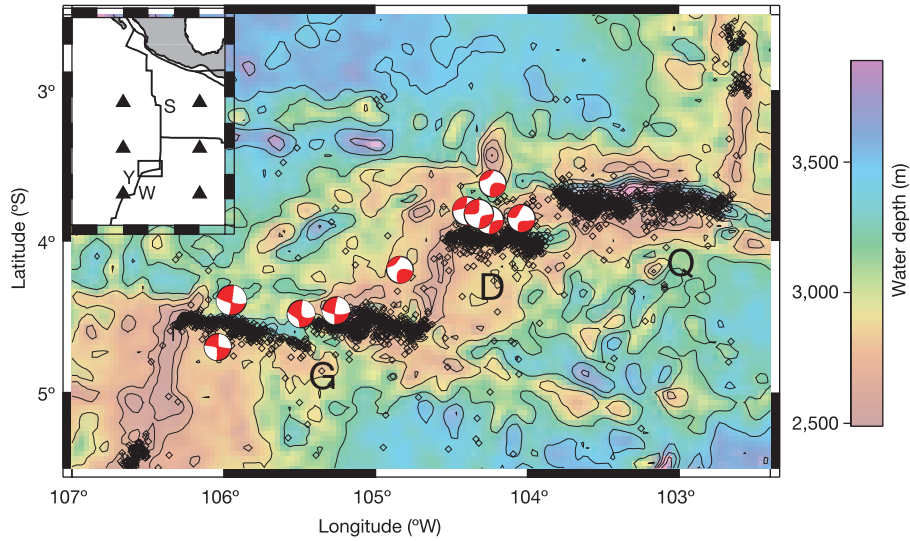


Figure 1 Map of the Quebrada (Q), Discovery (D), and Gofar (G) transform faults in the equatorial eastern Pacific, contoured with the bathymetry predicted from the satellite-derived gravity field⁴². Diamond symbols represent the acoustic radiator positions in the NOAA-PMEL seismicity catalogue for 1996–2001²⁴, and beachball symbols show the

focal mechanisms and centroid locations for the same period from the Harvard CMT catalogue. The inset map locates the EPR and Cocos ridge crests (black lines), the six NOAA hydrophones (triangles), the Wilkes (W), Yaquina (Y), and Siqueiros (S) transform faults, and the region of the main map (rectangle). The contour interval is 200 m.

an average rate of $\phi(m, t) = \rho(m)\psi(t)$, where t is time since the earthquake. This triggering rate is assumed to increase exponentially with magnitude, $\rho(m) = k \times 10^{\alpha(m-m_0)}$, where α is the triggering exponent, and to decay with time after a mother event according to the modified Omori law, $\psi(t) = \theta c^\theta / (c + t)^{1+\theta}$ (where $\theta > 0$). The constants k , θ and c are parameters that vary among regions. Renormalization for a single mainshock of magnitude m yields an average seismicity rate proportional to²⁹ $N_a^{II}(m) = \frac{k}{1-n} 10^{\alpha(m-m_0)}$. N_a^{II} is the expected number of aftershocks of any magnitude (type-II aftershocks; that is, not constrained to be smaller than m), and the constant $n = \int_0^1 \rho(\mu) dP(\mu) = kb/(b - \alpha)$ is the branching ratio, which equals both the average number of directly triggered aftershocks per event and the fraction of the earthquake population

that is made up of triggered earthquakes³⁰. The aftershock rate decays with an effective Omori exponent⁴ $p = 1 + O(\theta)$.

In the ETAS model, the seismicity rate before a mainshock at $t = 0$ increases according to the inverse Omori law; that is, $\sim |t|^{-p'}$, where $p' = 1 + O[\theta]$, and the expected number of events of all magnitudes conditioned on the mainshock occurrence (type-II foreshocks) is independent⁴ of m . This conditional foreshock number can be approximated as the product of two factors: the probability that the mainshock is a triggered event, and the expected number of events in a cluster averaged over mainshock magnitude. The first is just the branching ratio n , and the second is the integral $\int_0^1 N_a^{II}(\mu) dP(\mu)$; therefore³⁰, $N_f^{II} \approx n^2 / (1 - n)$. To include only earthquakes smaller than the mainshock (type-I foreshocks), we multiply the integrand by the probability that no event in a cluster exceeds m and integrate over the appropriate magnitude range. If $k/(1 - n)$ is small and m is large (conditions which apply to our data), then the extra probability factor is close to unity, and the results are $N_f^I \approx N_f^{II} [1 - 10^{-(b-\alpha)(m-m_0)}]$.

A similar modification to the aftershock number yields the foreshock/aftershock ratio:

$$\frac{N_f}{N_a} \approx n \left(\frac{b}{b - \alpha} \right) \left[\frac{10^{(b-\alpha)\Delta m_1^f} - 10^{(b-\alpha)\Delta m_2^f}}{10^{b\Delta m_1^a} - 10^{b\Delta m_2^a}} \right] \quad (1)$$

Here we have generalized the formula to count foreshocks in the magnitude range from $m - \Delta m_1^f$ to $m - \Delta m_2^f$ and aftershocks from $m - \Delta m_1^a$ to $m - \Delta m_2^a$, where $0 \leq \Delta m_2^{f,a} < \Delta m_1^{f,a} \leq m - m_0$. This approximation, which applies to large mainshocks, differs conceptually from the expression recently used by ref. 3 to explain the foreshock/aftershock ratios from global and regional catalogues (see Methods).

Anomalous foreshock activity

Earthquake populations on RTFs are well described by a tapered GR distribution having a low-magnitude slope $b \approx 1$ (refs 14, 15) similar to that of continental regions. The hydroacoustic catalogue for the EPR faults is consistent with this self-similar scaling, and its aftershock sequences decay according to Omori's law with³² $p \approx 1$, again similar to continental regions. However, global catalogues demonstrate that the aftershock productivity of large RTF earthquakes is lower than continental faults by approximately a factor of fifteen¹⁵ (Fig. 3). The low aftershock productivity combined with

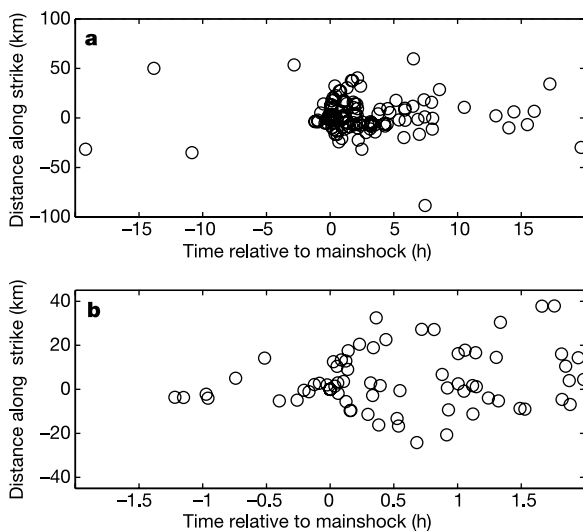


Figure 2 Space-time distribution of seismicity around the nine mainshocks ($M_w \geq 5.4$) on the Discovery and Gofar transform faults between May 1996 and December 2001, from the declustered Harvard CMT catalogue. **a**, Stack of all events from the NOAA-PMEL hydroacoustic catalogue with $M_{ASL} > 2.5$ (for $ASL > 207$) that were located within ± 100 km along strike and within ± 20 h of the mainshocks. Positive distance is west of the mainshock, and positive time is after the mainshock. **b**, Zoomed-in view of the same seismicity, showing foreshock activity within about 1 h and 15 km of the mainshocks.

the poor detection thresholds of global catalogues makes it difficult to constrain the values of n and α independently. A maximum-likelihood fit to the teleseismic RTF data yields a best-fit value of the triggering exponent $\alpha = 0.72$, and is consistent with the somewhat higher values found for California and Japan ($\alpha = 0.8\text{--}1.0$)^{33,34} (Fig. 3). Error bounds on the maximum-likelihood estimate are large, but aftershock counts using the hydroacoustic catalogue (points with horizontal bars in Fig. 3) also favour relatively high values of α and rule out values less than about 0.6 (see Supplementary Information).

The difference between oceanic and continental aftershocks primarily manifests itself in the intercept of the scaling relation, $k/(1-n)$, which is offset by about a factor of fifteen (Fig. 3). The maximum-likelihood fit in Fig. 3 corresponds to a branching ratio, $n \approx 0.1$, compared to values approaching unity in continental seismic zones³⁵. As discussed in the Supplementary Information, the aftershock rate may be somewhat higher for the EPR faults, but we can say with a high degree of confidence that $n < 0.3$. In other words, according to the ETAS model, most RTF earthquakes (70–90%) would be primary events driven by aseismic plate-tectonic loading rather than aftershocks of previous earthquakes. Equation (1) with the maximum-likelihood estimate of α and n predicts that the foreshock/aftershock ratio for RTFs should be about an order of magnitude lower than that observed in continents.

Instead, the EPR transform faults that are well recorded by the NOAA-PMEL array give values of N_f/N_a that are an order of magnitude higher than observed in Southern California (Fig. 4). For both regions, we identified mainshocks as events in the Harvard CMT catalogue with $M_w \geq 5.4$ that did not follow within 1 week and 100 km of another mainshock (see Methods), and we compiled

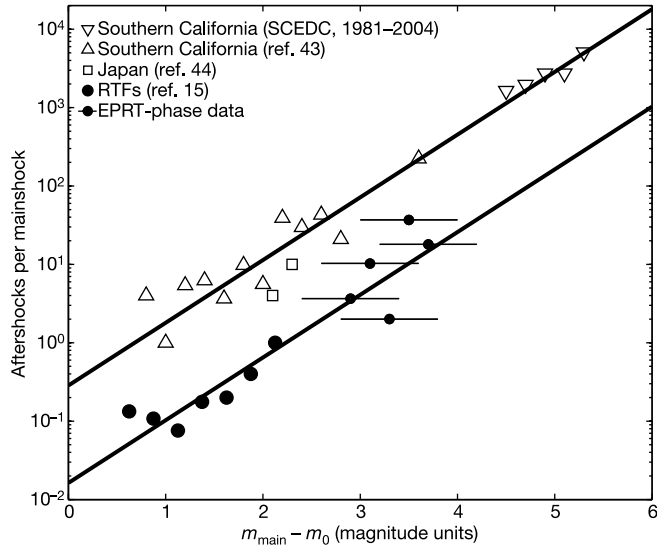


Figure 3 Aftershocks per mainshock, plotted against the difference between the mainshock magnitude m_{main} and the catalogue completeness threshold m_0 . RTF aftershocks (large filled circles) were defined as events with calibrated surface-wave magnitudes above $m_0 = 5.1$ that occurred within 14 days and 100 km of a $M_w \geq 5.6$ mainshock during the catalogue interval 1976–2001 (ref. 15). Southern California aftershocks from the SCEDC catalogue (open triangles) were defined as events above a local-magnitude (M_L) threshold of $m_0 = 2.0$ that occurred within 14 days and 100 km of a $M_L \geq 6.5$ mainshock during the interval 1981–2004. Aftershock counts from the EPR T -phase catalogue (small filled circles) are shown with error bars to account for uncertainties in m_0 ($2.0 \leq m_0 \leq 3.0$). The T -phase catalogue aftershocks were counted within 14 days and 30 km of the mainshocks. Previously published continental data sets (open triangles and squares) were compiled by Kisslinger and Jones⁴³ and Yamanaka and Shimazaki⁴⁴ using M_L thresholds of $m_0 = 4.0$ and 4.5 , respectively. Both RTF and continental aftershocks are consistent with a triggering exponent of $\alpha = 0.8$ (solid lines), but RTFs produce fewer aftershocks by a factor of fifteen.

foreshock and aftershock statistics from the NOAA-PMEL and the Southern California Earthquake Data Center (SCEDC) catalogues. We counted all events with local magnitudes (M_{ASL} or M_L) up to 2.8 units smaller than the mainshock M_w in the 1-h interval before and the 5-h interval after the mainshock. Figure 4 compares the observed N_f/N_a for spatial windows of various radii with the predictions of equation (1), corrected for the finite sampling intervals (see Methods). The SCEDC statistics satisfy an ETAS model with $\alpha = 0.8\text{--}0.9$, consistent with previous catalogue studies^{3,29}. However, foreshock rates from the NOAA-PMEL statistics are about two orders of magnitude greater than the ETAS predictions using the maximum-likelihood fit in Fig. 3. As shown in Fig. 4 and Supplementary Fig. S3, these results are robust with respect to the choice of windows and declustering procedures.

Therefore, we can reject the ETAS hypothesis that the clustering of foreshocks, mainshocks and aftershocks on RTFs can be described by the same seismic triggering mechanism. We infer that large earthquakes on EPR faults are preceded by an extended preparation process, possibly driven by subseismic transients (silent or quiet earthquakes), that can often be observed through foreshocks. This alternative hypothesis is consistent with the tightly localized distribution of the foreshocks about the mainshock in both space and time (Fig. 2 and Supplementary Fig. S4), which does not conform to the inverse-diffusive behaviour expected from the ETAS model⁴.

The correspondence of slow slip with foreshocks was suggested as early as 1976 by Kanamori and Stewart¹⁸, who noted a foreshock with a body-wave magnitude $m_b \approx 5$ about 500 s before the $M_w = 7$ slow earthquake on the Gibbs transform fault in the North Atlantic. More recently, McGuire *et al.* associated $m_b = 4.5\text{--}5.0$ foreshocks before the 1994 $M_w = 7.0$ Romanche²⁰ and 1997 $M_w = 6.8$ Prince Edward Island²¹ earthquakes with slow precursors observed at low frequencies. Forsyth *et al.*²² suggested

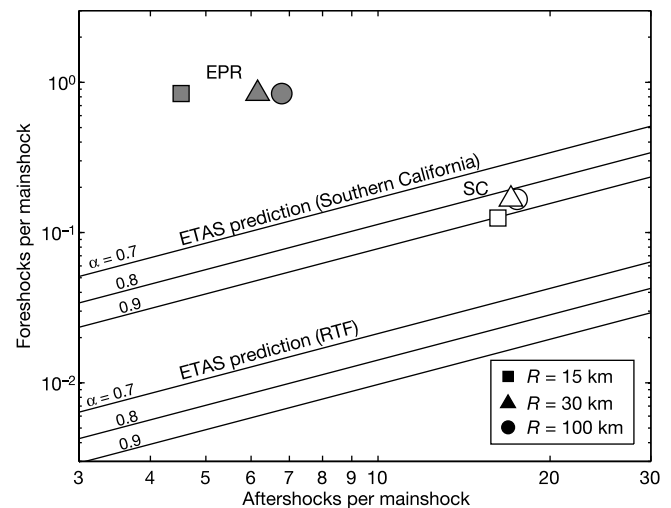


Figure 4 Foreshock and aftershock rates observed for EPR transform faults (solid symbols) and Southern California (open symbols) in regions of radius R about the mainshock. The data sets included 19 mainshocks ($M_w \geq 5.4$) on five transform faults (Discovery, Gofar, Wilkes, Yaquina and Siqueiros) from the declustered Harvard CMT catalogue for 1996–2001, and 24 mainshocks ($M_L \geq 5.4$) in Southern California from the declustered SCEDC catalogue for 1981–2003. Events with magnitudes up to 2.8 units below the mainshock magnitude were counted from the NOAA-PMEL and SCEDC catalogues in the 1-h window preceding and 5-h window following the mainshocks. These rates are compared with the N_f/N_a ratios from the ETAS model (equation (1)) for $\alpha = 0.7\text{--}0.9$ (solid lines), assuming $\Delta m_2^{f,a} = 0$, $\Delta m_1^{f,a} = 2.8$ and $b = 1$, with estimated branching ratios of $n = 0.8$ (Southern California) and $n = 0.1$ (RTF). The $\alpha = 0.8$ line for RTFs is close to the maximum-likelihood estimate from Fig. 3. Uncertainties in α and n allow shifts in the ETAS prediction upwards from the maximum-likelihood value by half an order of magnitude at most.

articles

that a subseismic slip process was responsible for a swarm of contemporaneous seismicity on the Anakena and Raraku transform faults of the southern EPR recorded by an ocean-bottom seismometer array in 1995. These and other examples³⁶ combined with the global aftershock depletion (Fig. 3) and the evidence for slow precursors to large earthquakes on RTFs worldwide¹⁹, indicate that the aseismic, foreshock-generating process on EPR faults may be prevalent throughout the mid-ocean-ridge system, including the slower-slipping, colder RTFs in the Atlantic and Indian oceans.

Short-term predictability of large earthquakes

The high rate of proximate foreshocks suggests a naive scheme for short-term earthquake prediction—we simply assume that every event is a foreshock of an impending large earthquake. We can formalize this scheme into a well-posed prediction algorithm³⁷: whenever we observe any RTF event above some ASL magnitude threshold m_0 within a specified RTF region, we issue an alert that an earthquake of moment magnitude greater than or equal to m_p will occur sometime during time window of length t_p immediately following the event and somewhere in a spatial window of radius r_p about the event's epicentre. Figure 5 illustrates this prediction algorithm for the parameter set [$m_0 = 2.5$ (M_{ASL}), $m_p = 5.4$ (M_W), $t_p = 1$ h, $r_p = 15$ km] by applying it retrospectively to the two most active EPR transform faults, Discovery and Gofar. Of the nine candidate earthquakes that occurred during the catalogue interval May 1996–November 2001, six were located within the space-time prediction windows (Fig. 5) and thus constitute successful predictions. There were three failures-to-predict and about 1,400 false alarms.

Although the false-alarm rate is quite high, all alarms taken together occupy only about 0.15% of the total space-time volume of about 250 km \times 5.5 yr (see Supplementary Information). We can relate $P(M|F)$, the probability of a mainshock M in the prediction window given the occurrence of a foreshock F , to $P(M)$, the probability of M in a random window of the same size, using the Bayes identity:

$$P(M|F) = P(M) \left[\frac{P(F|M)}{P(F)} \right] \quad (2)$$

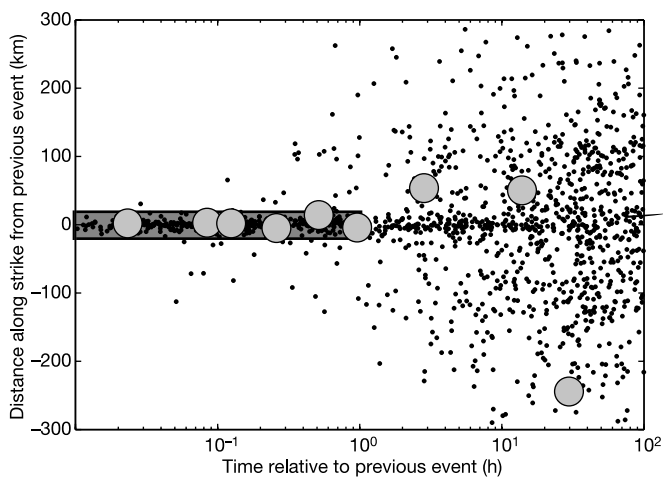


Figure 5 Retrospective application of the naive prediction algorithm described in the text to the NOAA-PMEL catalogue (May 1996–November 2001) for the Discovery and Gofar faults. Plot shows along-strike distance (positive to the west) and time of each earthquake relative to its previous event for all catalogued events with $M_{ASL} \geq 2.5$ ($ASL \geq 207$). Events were considered to be distinct if they were separated by more than 1 min from the previous event, to exclude redundancies. Six of the nine mainshocks identified from the declustered Harvard CMT catalogue (large circles) fall within the 1-h, ± 15 -km alert windows (shaded area) used in the prediction algorithm.

$P(F|M)$ is the fraction of mainshocks preceded by foreshocks, and $P(F)$ equals the fraction of the space-time volume occupied by alerts. The ratio of these probabilities (the term in square brackets) is the probability gain factor g of the prediction algorithm³⁷. Our retrospective analysis of the Discovery and Gofar faults gives $g = 450$. This performance can be compared to prediction experiments in California, where even highly optimized algorithms with many adjustable parameters are thought to achieve probability gains of 10–20 or less³⁸.

The performance relative to random chance can be evaluated using Molchan's³⁹ error diagram, which plots the failure-to-predict probability, $1 - P(F|M)$, against $P(F)$ (Fig. 6). Large sets of random alerts should fall close to the line $1 - P(F)$, corresponding to no probability gain ($g = 1$). Figure 6 shows that the Discovery–Gofar point lies well below the 99% confidence range for random chance; the probability of reproducing this performance with random alerts filling 0.15% of the space-time volume is less than one in ten million. Similar results were obtained by applying the algorithm retrospectively to the five active EPR transforms in the study area; nine of sixteen mainshocks were successfully predicted by alerts occupying 0.13% of the space-time volume, which gives $g = 340$ (Fig. 6, see Supplementary Discussion).

Our naive algorithm is far from optimal. For instance, raising the threshold magnitude m_0 from 2.5 to 3.4 (that is, increasing the ASL from 207 to 215) reduces the number of alarms in the Gofar–Discovery catalogue to 407 without changing $P(F|M)$, increasing g to about 1,000 (Fig. 6). More parameters could be added to improve the performance further.

Discussion

Mid-ocean ridges are far removed from urban centres on continents, so the direct societal value of short-term earthquake prediction on RTFs (assuming it could be operationally implemented using real-time, near-source monitoring) would be small. Nevertheless, the existence of short-term predictability in this tectonic environment—the main conclusion of this paper—is of considerable scientific interest, because it supports a physical linkage between foreshocks and mainshocks through stress changes driven by aseismic slip transients or some other fault preparation process

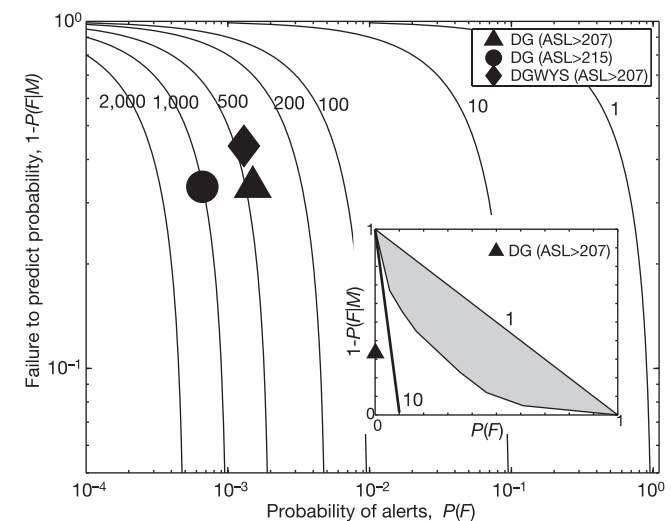


Figure 6 Molchan's³⁹ error diagram of the failure-to-predict probability $1 - P(F|M)$ against the probability of alerts $P(F)$ on a logarithmic scale, contoured with probability gain g (solid curves). Performance of the naive prediction algorithm is given for the Discovery and Gofar (DG) faults with $m_0 = 2.5$ (triangle) and $m_0 = 3.4$ (circle), and for the five active EPR faults (DGWYS) with $m_0 = 2.5$ (diamond). Inset diagram is the same plot on a linear scale, comparing the 99% confidence region for a random prediction of nine mainshocks (shaded area) with the first DG test (triangle).

such as hydrothermal flow or nearby magmatic activity.

To monitor RTFs geodetically will require a new generation of ocean-bottom instrumentation, a considerable technological challenge. But collecting such data may well be the best way to test the hypothesis that three anomalous aspects of RTF seismicity—large slip deficits, high foreshock activity and slow earthquakes—can be explained by aseismic fault-slip transients. Given the importance of understanding the fundamental mechanics of earthquake predictability, overcoming the technological hurdles should be worth the effort. □

Methods

We use the NOAA-PMEL hydroacoustic earthquake catalogue for the equatorial Pacific which began in 1996 (ref. 24). Their array (Fig. 1) records acoustic energy radiated into the water column by earthquakes and other sources (T -phases). T -phases propagate very efficiently in the low-velocity sound fixing and ranging (SOFAR) channel, and the array arrivals can be used to locate precisely where the energy entered the SOFAR channel. The standard errors in this source location are estimated to be ± 2 km, ± 10 s for the southern/northernmost faults (the Wilkes and Siqueiros faults) and are slightly smaller for the faults located in the centre of the array²⁴ (the Discovery and Gofar faults). A propagation model is used to convert the magnitude of the pressure signal at the hydrophones into an ASL (measured in decibels) at the source location. We used a conversion between ASL and magnitude, $M_{ASL} = 0.107ASL - 19.6$, obtained from the regression of the observed ASLs compiled in ref. 32 against the body-wave magnitudes of the International Seismological Centre (ISC) catalogue (<http://www.isc.ac.uk/>). Frequency-magnitude statistics indicate that the seismicity catalogues are approximately complete down to $ASL \approx 207$ – 212 , or $M_{ASL} \approx 2.5$ – 3.0 .

To prevent biases from ongoing aftershock sequences, we eliminated CMT catalogue earthquakes that occurred within 1 week and 100 km of a previous CMT earthquake from our analysis. Our de-clustering criterion eliminated only one earthquake with $M_w \geq 5.5$ from the Discovery–Gofar set and only two from the mainshock set for other three active RTFs within the NOAA-PMEL array. Moderate increases in the space and time windows did not disqualify additional events. Moreover, each of the three disqualified events had a foreshock sequence distinct from the aftershock sequence of the preceding mainshock, consistent with the statistics in Fig. 4 (see Supplementary Fig. 2).

The time dependence of foreshock and aftershock rates in ETAS is controlled by Omori's law. Helmstetter *et al.*⁴ have demonstrated that the time-decay exponent p in the renormalized Omori law is not strictly a constant. When $\rho(m)$ has finite variance ($\alpha/b \leq 1/2$), p varies from $1 - \theta$ for $t \ll t^* = c(n/1 - n_1)^{1/\theta}$ to $1 + \theta$ for $t \gg t^*$. The theory breaks down for $\alpha/b > 1/2$, owing to the strong coupling between earthquake energy and seismicity rate, but the numerical simulations of ref. 4 indicate that the short-time value of p increases approximately linearly from $1 - \theta$ at $\alpha/b = 1/2$ to $1 + \theta$ as $\alpha/b \rightarrow 1$. For $\alpha/b = 0.8$, the Omori exponents can be approximated by $p' \approx p \approx 1 + \theta$; hence, the requisite integrals are $\int_0^{\Delta t_{f,a}} \psi(\tau) d\tau \approx 1 - (c/\Delta t_{f,a})^\theta$, where the approximation assumes $\Delta t_{f,a} \gg c$. Equation (1) can thus be corrected for the finite foreshock and aftershock sampling intervals, $\Delta t_f = 1$ h and $\Delta t_a = 5$ h, by multiplying its right-hand side by the ratio of these integrals. This ratio varies from 0.72 to 0.94 over the plausible range of parameters $c = 1$ s – 1 min, $\theta = 0$ – 0.2 , so the correction is minor.

Equation (1) is a more general form of models used in previous studies^{3,12,40,41}. Feltzer *et al.*³ consider the case $\alpha = b$. Taking this limit in equation (1), we obtain $N_f/N_a \approx n(\ln 10) \left[\frac{\Delta m_f^2 - \Delta m_a^2}{10^{0.25\Delta m_f^2} - 10^{0.25\Delta m_a^2}} \right]$. For the magnitude ranges of ref. 3 ($\Delta m_f^2 = 1.0$, $\Delta m_a^2 = 0$; $\Delta m_f^2 = 1.0$, $\Delta m_a^2 = 0.4$), the ratio in brackets reproduces their foreshock/aftershock ratio of 0.134. The factor $n(\ln 10)$ missing in their equation (6) probably lies between 1 and 2 for continental and subduction-zone seismicity³⁰, so their formula provides an adequate approximation in most regions. For RTFs, however, the scaling of N_f/N_a with the branching ratio n is numerically important (see Fig. 4).

Received 3 September 2004; accepted 19 December 2005; doi:10.1038/nature03377.

- Jones, L. M. & Molnar, P. Some characteristics of foreshocks and their possible relationship to earthquake prediction and premonitory slip on faults. *J. Geophys. Res.* **84**, 3596–3608 (1979).
- Abercrombie, R. E. & Mori, J. Occurrence patterns of foreshocks to large earthquakes in the Western United States. *Nature* **381**, 303–307 (1996).
- Felzer, K., Abercrombie, R. E. & Ekstrom, G. A common origin for aftershocks, foreshocks, and multiplets. *Bull. Seismol. Soc. Am.* **94**(1), 88–98 (2004).
- Helmstetter, A., Sornette, D. & Grasso, J.-R. Mainshocks are aftershocks of conditional foreshocks: How do foreshock statistical properties emerge from aftershock laws. *J. Geophys. Res.* **108**, doi:10.1029/2002JB001991 (2003).
- Dodge, D. A., Ellsworth, W. E. & Beroza, G. C. Detailed observations of California foreshock sequences: Implications for the earthquake initiation process. *J. Geophys. Res.* **101**, 22371–22392 (1996).
- Geller, R. J., Jackson, D. D., Kagan, Y. Y. & Mulargia, F. Earthquakes cannot be predicted. *Science* **275**, 1616–1617 (1997).
- Hirose, H., Hirahara, K., Kimata, F., Fujii, N. & Miyazaki, S. A slow thrust slip event following the two 1996 Hyuganada earthquakes beneath the Bungo Channel, Southwest Japan. *Geophys. Res. Lett.* **26**, 3237–3240 (1999).
- Ozawa, S. *et al.* Detection and monitoring of ongoing aseismic slip in the Tokai region, central Japan. *Science* **298**, 1009–1012 (2002).
- Ozawa, S. *et al.* Characteristic silent earthquakes in the eastern part of the Boso peninsula, Central Japan. *Geophys. Res. Lett.* **30**, doi:10.1029/2002GL016665 (2003).
- Dragert, H., Wang, K. & James, T. S. A silent slip event on the deeper Cascadia subduction interface. *Science* **292**, 1525–1528 (2001).

- Kanamori, H. & Cipar, J. Focal process of the great Chilean earthquake. *Phys. Earth Planet. Inter.* **9**, 128–136 (1974).
- Reasenber, P. A. Foreshock occurrence before large earthquakes. *J. Geophys. Res.* **104**, 4755–4768 (1999).
- Brune, J. N. Seismic moment, seismicity, and rate of slip along major fault zones. *J. Geophys. Res.* **73**, 777–784 (1968).
- Bird, P., Kagan, Y. & Jackson, D. in *Plate Boundary Zones* (ed. Freymueller, S. S. A. J.) 203–218 (AGU, Washington DC, 2002).
- Boettcher, M. S. & Jordan, T. H. Earthquake scaling relations for mid-ocean ridge transform faults. *J. Geophys. Res.* **109**, doi:10.1029/2004JB003110 (2004).
- Bird, P. & Kagan, Y. Plate-tectonic analysis of shallow seismicity: Apparent boundary width, beta, corner magnitude, coupled lithosphere thickness, and coupling in 7 tectonic settings. *Bull. Seismol. Soc. Am.* **94**(6), 2380–2399 (2004).
- Perez-Campos, X., McGuire, J. J. & Beroza, G. C. Resolution of the slow earthquake/apparent stress paradox for oceanic transform fault earthquakes. *J. Geophys. Res.* **108**, doi:10.1029/2002JB002312 (2003).
- Kanamori, H. & Stewart, G. S. Mode of strain release along the Gibbs fracture zone, Mid-Atlantic Ridge. *Phys. Earth Planet. Inter.* **11**, 312–332 (1976).
- Ihmlé, P. F. & Jordan, T. H. Teleseismic search for slow precursors to large earthquakes. *Science* **266**, 1547–1551 (1994).
- McGuire, J. J., Ihmlé, P. F. & Jordan, T. H. Time-domain observations of a slow precursor to the 1994 Romanche transform earthquake. *Science* **274**, 82–85 (1996).
- McGuire, J. J. & Jordan, T. H. Further evidence for the compound nature of slow earthquakes: The Prince Edward Island earthquake of April 28, 1997. *J. Geophys. Res.* **105**, 7819–7828 (2000).
- Forsyth, D. W., Yang, Y., Mangriots, M.-D. & Shen, Y. Coupled seismic slip on adjacent oceanic transform faults. *J. Geophys. Res.* **30**, doi:10.1029/2002GL016454 (2003).
- Abercrombie, R. E. & Ekstrom, G. Earthquake slip on oceanic transform faults. *Nature* **410**, 74–77 (2001).
- Fox, C. G., Matsumoto, H. & Lau, T. K. Monitoring Pacific Ocean seismicity from an autonomous hydrophone array. *J. Geophys. Res.* **163**, 4183–4206 (2001).
- Fox, C. G. *et al.* Acoustic detection of seafloor spreading. *J. Geophys. Res.* **22**, 131–134 (1995).
- Smith, D. *et al.* Hydroacoustic monitoring of seismicity at the slow-spreading Mid-Atlantic Ridge. *Geophys. Res. Lett.* **29**, 10.1029/2001GL013912 (2002).
- McGuire, J. J. Immediate foreshock sequences of oceanic transform earthquakes on the East Pacific Rise. *Bull. Seismol. Soc. Am.* **93**, 948–952 (2003).
- Ekstrom, G., Dziewonski, A. M., Maternovskaya, N. N. & Nettles, M. Global seismicity of 2001: centroid-moment tensor solutions for 961 earthquakes. *Phys. Earth Planet. Inter.* **136**, 165–185 (2003).
- Helmstetter, A. & Sornette, D. Bath's law derived from the Gutenberg–Richter law and from aftershock properties. *Geophys. Res. Lett.* **30**, doi:10.1029/2003GL018186 (2003).
- Helmstetter, A. & Sornette, D. Importance of direct and indirect triggered seismicity in the ETAS model of seismicity. *Geophys. Res. Lett.* **30**, 4, doi:10.1029/2003GL017670 (2003).
- Ogata, Y. Statistical models for earthquake occurrence and residual analysis for point processes. *J. Am. Stat. Assoc.* **83**, 9–27 (1988).
- Bohnenstiehl, D. R., Tolstoy, M., Dziak, R. P., Fox, C. G. & Smith, D. Aftershocks in the mid-ocean ridge environment: An analysis using hydroacoustic data. *Tectonophysics* **354**, 49–70 (2002).
- Helmstetter, A. Is earthquake triggering driven by small earthquakes? *Phys. Rev. Lett.* **91**, 058501 (2003).
- Helmstetter, A., Kagan, Y. & Jackson, D. D. Importance of small earthquakes for stress transfers and earthquake triggering. *J. Geophys. Res.* (in press).
- Helmstetter, A. & Sornette, D. Subcritical and supercritical regimes in epidemic models of earthquake aftershocks. *J. Geophys. Res.* **107**, doi:10.1029/2001JB001580 (2002).
- Hanson, J. A. & Given, H. K. Accurate azimuth estimates from a large aperture hydrophone array using T-phase waveforms. *Geophys. Res. Lett.* **25**, 365–368 (1998).
- Aki, K. in *Earthquake Prediction* (eds Simpson, D. W. & Richards, P. G.) 556–574 (AGU, Washington DC, 1981).
- Keilis-Borok, V., Shebalin, P., Gabrielow, A. & Turcotte, D. Reverse tracing of short-term earthquake precursors. *Phys. Earth Planet. Inter.* **145**, 75–85 (2004).
- Molchan, G. M. Earthquake prediction as a decision-making problem. *Pure Appl. Geophys.* **149**, 233–247 (1997).
- Reasenber, P. A. & Jones, L. M. Earthquake hazards after a mainshock in California. *Science* **243**, 1173–1176 (1989).
- Reasenber, P. A. & Jones, L. M. Earthquake aftershocks: Update. *Science* **265**, 1251–1252 (1994).
- Sandwell, D. T. & Smith, W. H. F. Marine gravity anomaly from Geosat and ERS 1 satellite altimetry. *J. Geophys. Res.* **102**, 10039–10054 (1997).
- Kisslinger, C. & Jones, L. M. Properties of aftershock sequences in Southern California. *J. Geophys. Res.* **96**, 11947–11958 (1991).
- Yamanaka, Y. & Shimazaki, K. Scaling relationship between the number of aftershocks and the size of the main shock. *J. Phys. Earth* **38**, 305–324 (1990).

Supplementary Information accompanies the paper on www.nature.com/nature.

Acknowledgements We thank R. Dziak for answering questions about details of the hydroacoustic earthquake catalogues, D. Bohnenstiehl for suggestions on clarifying the manuscript, A. Helmstetter for her help in understanding ETAS, and V. Keilis-Borok, I. Zaliapin, and L. Jones for discussions of earthquake prediction algorithms. J.J.McG. was supported by the Frank and Lisina Hoch Fund. M.S.B. was supported by the Deep Ocean Exploration Institute at WHOI. This work was supported by the NSF, SCEC and USGS.

Competing interests statement The authors declare that they have no competing financial interests.

Correspondence and requests for materials should be addressed to J.J.McG. (jmcguire@whoi.edu).